metals

MDPI

Article

Optimizing the Gating System for Rapid Investment Casting of Shape Memory Alloys: Computational Numerical Analysis for Defect Minimization in a Simple-Cubic Cell Structure

Carlos E. S. Albuquerque [1], Paulo C. S. Silva [2], Estephanie N. D. Grassi [2], Carlos J. De Araujo [2], João M. P. Q. Delgado [3,*] and Antonio G. B. Lima [2]

[1] Production Engineering Council, Federal University of the Vale do São Francisco, Campus Salgueiro, Rua Antônio Figueira, 134, Salgueiro 56000-000, PE, Brazil; carlos.albuquerque@univasf.edu.br
[2] Department of Mechanical Engineering, Center of Science and Technology, Federal University of Campina Grande, Rua Aprígio Veloso, 882, Campina Grande 58429-900, PB, Brazil; paulocesarsales@outlook.com (P.C.S.S.); end.grassi@hotmail.com (E.N.D.G.); carlos.jose@professor.ufcg.edu.br (C.J.D.A.); antonio.gilson@ufcg.edu.br (A.G.B.L.)
[3] CONSTRUCT-LFC, Civil Engineering Department, Faculty of Engineering, University of Porto, 4200-465 Porto, Portugal
* Correspondence: jdelgado@fe.up.pt; Tel.: +351-225081404

Abstract: With the aid of virtual prototyping and casting numerical simulation, this work presents the optimization of an injection system used in a non-traditional investment casting process that applies perpendicular centrifugal force to inject the molten metal into refractory plaster molds. In this study, advanced techniques of simulation and production of complex geometries in Computer-Aided Design CAD (Computer-Aided Design) are used in the design of the casting system of a miniaturized simple-cubic cell structure. The cast part has a complex shape profile and needs a high surface finish with strict dimensional tolerance. The alloy used to fill the mold is an aluminum bronze shape memory alloy (SMA). CAD was used to model the part and the proposed models for casting optimization. ProCAST software was used for the numerical simulation of the casting process. Experimental parameters were used as input data for the numerical simulation. The simulation results were analyzed focusing on the identification of defects in the Cu–Al–Mn SMA simple-cubic structures. Different feeding systems have been designed to eliminate the identified defects. Concerning the molten recirculation, the optimal nozzle model has a truncated cone profile, with a larger radius of 6.5 mm, a smaller radius of 2.0 mm and a height of 8.0 mm (called here model 3). Experimental observations from cast SMA parts agree with the simulated results of the optimized nozzle model 3. In addition to the elimination of alloy recirculation with the nozzle optimization in this work, the shrinkage porosity at the upper base of the part was eliminated with the addition of a compensation volume close to the region where porosity is more intense. By exploring the possibilities offered by commercial software, the work contributes to advance the knowledge and application of the non-traditional investment casting process, highlighting its advantages and potential applications.

Keywords: casting numerical simulation; investment casting; SMA; ProCAST; virtual prototyping

check for updates

Citation: Albuquerque, C.E.S.; Silva, P.C.S.; Grassi, E.N.D.; De Araujo, C.J.; Delgado, J.M.P.Q.; Lima, A.G.B. Optimizing the Gating System for Rapid Investment Casting of Shape Memory Alloys: Computational Numerical Analysis for Defect Minimization in a Simple-Cubic Cell Structure. *Metals* **2023**, *13*, 1138. https://doi.org/10.3390/met13061138

Academic Editor: Alexander V. Shelyakov

Received: 25 April 2023
Revised: 6 June 2023
Accepted: 16 June 2023
Published: 19 June 2023

Copyright: © 2023 by the authors. Licensee MDPI, Basel, Switzerland. This article is an open access article distributed under the terms and conditions of the Creative Commons Attribution (CC BY) license (https://creativecommons.org/licenses/by/4.0/).

1. Introduction

Metal cellular lattice structures (CLSs) have attracted much attention in biomedical (e.g., metallic implants) and industrial (e.g., aircraft fuselage and wings) applications due to their combination of mechanical, thermal and acoustic properties, creating opportunities for diverse cross-functional structural implementations [1]. These include ultralight structures with high specific strength [2,3] and stress [4] and excellent impact absorption [5]. While CLSs can be manufactured as stochastic and periodic patterns, periodic CLSs have superior characteristics over stochastics; hence, their use in high-value engineering products is

preferred [6,7]. In addition, the mechanical properties of periodic CLSs can be adjusted to the required level, which is not the case with stochastic structures [8]. So far, different types of periodic CLSs have been investigated, including octet trusses [9], triangulated faces of flat trusses [10], central pyramidal structure [10], simple-cubic and body-centered cell structure (BCC) [11], BCC-Z [11], F2FCC [11] and F2FCC-Z [11].

Different materials have been used to produce CLSs, including stainless steel, Ti-6Al-4V and NiTi [12,13]. NiTi, also known as Nitinol, is by far the most applied shape memory alloy (SMA). SMA belong to a material class called intelligent or smart, which are a group of new, state-of-the-art materials, that, over the last decades, have been developed and applied in various sectors. Smart materials are capable of sensing changes in their environment and responding to these changes in a predetermined way. SMA have the ability to return to a predetermined shape after a pseudoplastic deformation through simple heating, which is called shape memory effect (SME). On the other hand, the ability to recover large strains (8% under isothermal tension) after a simple mechanical unloading is called superelasticity or pseudoelasticity (SE) [14]. In addition, both phenomena are associated with a mechanical hysteresis, which benefits dampening and shock absorption applications. There are two main SMA composition groups: Ni–Ti-based alloys (Ni–Ti–Cu, Ni–Ti–Mo, Ni–Ti–Nb, etc.) and Copper-based alloys (Cu–Zn–Al, Cu–Al–Ni, Cu–Al–Mn, Cu–Al–Be, etc.). Cu–Al-based alloys have not only the functional characteristics of shape memory effect (SME) and superelasticity (SE) but also are low cost and easier to manufacture compared to Ni–Ti-based alloys [15]. Therefore, in addition to a high strength-to-weight ratio, relatively low mass, low heat conductivity, high energy absorption and appropriate thermal and sound insulation properties, CLSs made with SMA offer other benefits such as shape memory properties [16,17], superelastic behavior [18] and low modulus of elasticity [19,20].

Until now, several conventional techniques have been applied to produce CLSs, including casting, additive manufacturing and mechanical forming [21]. According to Mun et al. [22], metal additive manufacturing processes that use laser or electron beam on a metallic powder are completely capable of manufacturing complex 3D metallic CLSs. Additive metal manufacturing methods consist of progressively depositing layers, one on top of the other, until forming an object, following a 3D digital model. It is a relatively recent technology, developed in the 1990s, which enabled new features such as rapid prototyping, manufacturing of parts with complex geometries and customization of components that would be difficult to manufacture by conventional routes [23].

However, despite these advantages, there are still restrictions in the process. Metal parts produced by additive manufacturing are known to have macroscale defects such as unmelted powder (i.e., lack of fusion), porosity, delamination and distortion [24–29]. On a microstructural scale, metal additive manufacturing processes are associated with extreme temperature variations in their melting and solidification cycles [30]. Consequently, they can generate parts with grains of different morphologies and anisotropic behavior dependent on the construction direction [29,31–33]. This heterogeneous microstructure can be further accentuated by cyclic recrystallization during repeated layer deposition [26].

Metal casting, on the other hand, allows for excellent microstructural and dimensional control [34–38]. The investment casting process aided by 3D printing techniques is an advantageous alternative for the production of CLSs manufactured with SMA. The investment casting process is one of the preferred casting methods used to produce components with low dimensional tolerance, high degree of precision and excellent surface finish. Even though it is a precision manufacturing process, at each manufacturing stage the investment casting is subject to design and processing errors, resulting in defects in the obtained piece. Casting defects are discontinuities that do not conform to design requirements with respect to geometry (mismatches, undulations or dimensional defects); integrity (porosity, cracks, oxides and inclusions); and material properties (hardness and mechanical resistance below the specified standards). Broadly, defects in castings can be allocated into four categories: filling defects; shape-related defects; thermal and appearance defects. Correctly identifying such casting defects in the initial manufacturing phases significantly reduces the probability

of product failure, raw materials expenditure, the release of gases into the environment, and energy and time consumption. There are several ways to analyze the phenomena that occur in the casting process, among which stand out real casting tests and process numerical simulation. The later allows a much faster and cheaper analysis and is an advantageous technique used to reduce the risk of defects. Simulation technologies are applied extensively in casting industries to understand the effects of physical phenomena such as chemical changes, phase transformation, heat transfer, fluid flow, microstructural evolution and mechanical stresses on defect formation and final mechanical properties [39].

Although all casting processes are subject to design and processing errors, an early and correct identification of defects significantly reduces the probability of product failure. In this sense, numerical simulation of the casting process is an advantageous technique used to reduce the risk of defects. Simulation technologies are applied extensively in foundry industries to understand the effects of physical phenomena such as chemical variation, phase transformation, heat transfer, fluid flow, microstructural evolution and mechanical stresses on defect formation and final mechanical properties [39].

Numerical simulation of the casting and solidification consists of virtually reproducing processes such as filling, solidification, defect formation and distribution characteristics during the casting, which allows predictions and adjustments before performing real experiments. For this purpose, a detailed knowledge of the casting and solidification process is necessary, including the behavior of the material as a function of temperature, the microstructural behavior of the material, the interactions between mold and material and the appropriate calculation methods to represent the phenomena involved.

Virtual casting analysis has gained increasing attention in the scientific community due to its advantages in terms of cost-effectiveness, shorter analysis time and reduced environmental impact compared to real casting tests. Several authors have contributed to this field by publishing studies employing numerical simulation to investigate fluid flow, solidification and defect formation in each stage of the casting process, including filling, injection and solidification [40–45]. These research efforts have played a significant role in advancing knowledge in this area and improving casting processes. Furthermore, it is worth mentioning the utilization of the ProCAST® finite element software by researchers, such as the authors [46–51], to conduct these studies.

In this context, this work proposes a computational analysis of a non-traditional rapid investment casting process that applies perpendicular centrifugal force to inject the molten metal inside refractory plaster molds. Despite its relevance, the process is not well-explored in the literature, offering a wide field to be explored. Therefore, this study's main contributions are the application of a non-traditional centrifugal precision casting process coupled with the analysis of an alloy with distinct functional properties. By exploring the possibilities offered by commercial software, the work seeks to advance the knowledge and application of this casting method, highlighting its advantages and potential applications.

In a previous work [52], the potential of applying computational numerical analysis methods combined with the fabrication of SMA by non-conventional precision casting was used to study the castability of copper-based SMA, making it possible to estimate interface heat transfer coefficients (IHTC). In this work, the analysis focuses on the manufacture of a topologically optimized structure with complex geometry that requires great dimensional tolerance and the absence of porosity defects that can harm the mechanical properties of the part. The optimized functional structures are designed to allow experimental tests to aid the development of vibration control devices. The topology of the cells is simple-cubic, and the analysis is carried out with the aid of the ProCAST software. The virtual prototyping analysis is used to optimize the molten metal injection system in the molds, thus reducing defects and filling time of the Cu–Al–Mn SMA presenting the SME.

2. Methodology

The methodology used in this work is summarized in the flowchart of Figure 1. The optimization process was divided in two steps: firstly focusing on the solution of

recirculation during injection and afterwards solving the recurrent porosity on the upper base of the desired casting geometry.

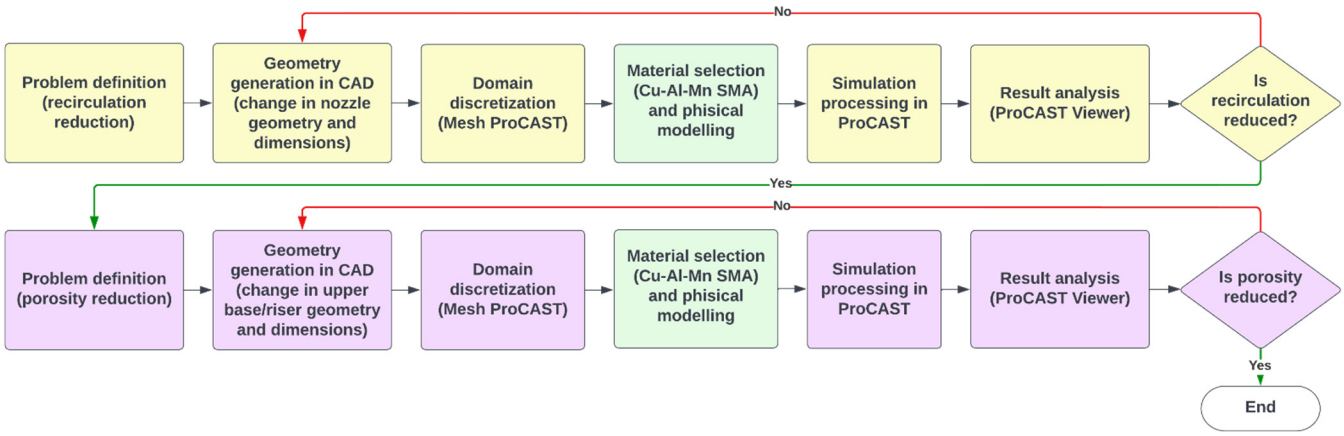


Figure 1. Methodology flowchart.

The addressed problem deals with the simulation of the filling, solidification and defect formation process of a Simple-Cubic (SC) metallic cellular lattice structure using the ProCAST software (Version 16, ESI, Paris, França). The casting process chosen for the study uses centrifugal force as a means of forcing the molten metal into the mold. Figure 2a schematically illustrates the simulated casting method for the production of miniaturized shape memory alloy components with the Power Cast 1700 equipment [53]. Figure 2b shows the part and mold design used in this study. The mold has a cylindrical shape with 50 mm in diameter and 70 mm in height. The SC unit cell structure has a strut diameter and length of 1 mm and 2.5 mm, respectively. A fillet radius of 0.4 mm was used on the coincident edges. The lattice structure was generated by repeating 5, 7 and 5 unit cells in the x, y and z directions, respectively, with a spacing of 2 mm, resulting in a porosity of approximately 59% (with respect to a dense rectangular block of 10.5 × 14.5 mm). In addition, dense blocks were added at the ends of the SC lattice structure, measuring 10.5 mm of side and 3 mm of thickness.

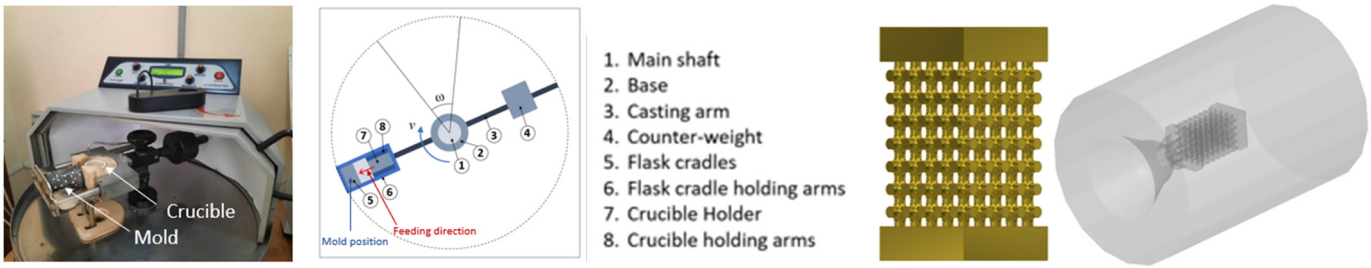


Figure 2. (**a**) Inside picture of the PowerCast 1700 equipment and illustration of the centrifuge system used in the studied casting process. (**b**) CAD of the studied part and mold.

The purpose of the analysis presented in this work is to reduce alloy loss by recirculation, reduce the possibility of damage to the crucible tip and increase the efficiency of the mold-filling flow. The model originally used to inject the desired cellular compression structure shows signs of expulsion in counterflow from the alloy to the interior of the equipment, and in many cases, the piece is joined to the crucible, leading to the loss of the crucible tip. Figure 3 shows an example of such a joining between the part and the mold generated during the injection.

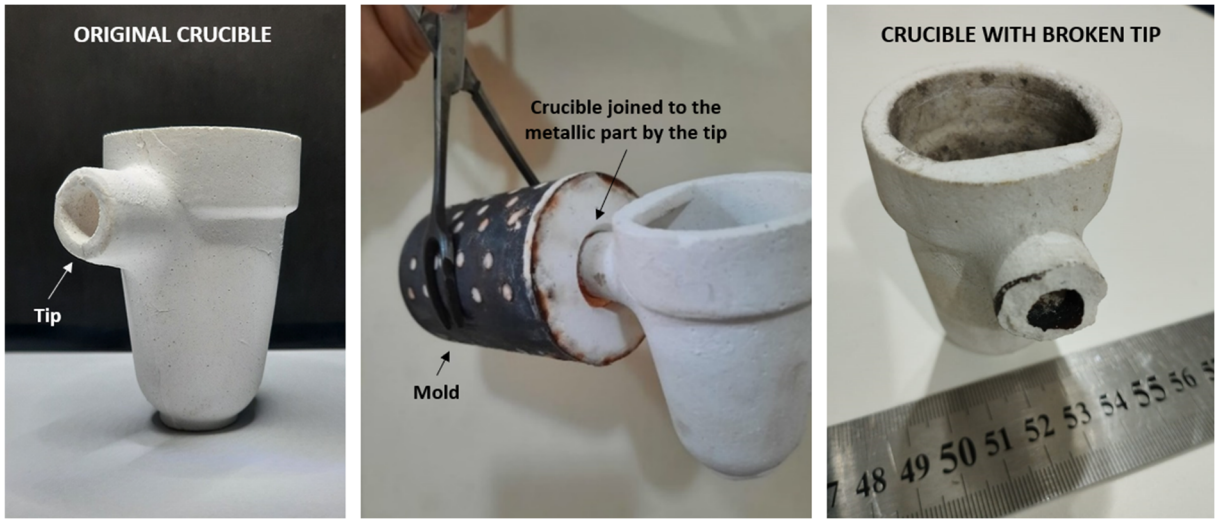


Figure 3. Example of the joining between the part and the mold generated by the recirculation of the alloy and the consequent tip fracture.

The converging nozzle studied in this work is divided in two parts. The first is a standard base used to support the parts in the mold. This base is 3D printed in polylactic acid (PLA) and measures 12 mm in height, 24 mm in the larger diameter and 13 mm in the smaller diameter. It was kept unchanged throughout the evaluated cases. The second part of the nozzle originally has the shape of a half-sphere with a diameter of 13 mm, but for the optimization study, this profile will be replaced by more efficient profiles in relation to the fluid flow. Therefore, for the analysis of virtual prototyping, four models of parts with simple-cubic geometry cell-structure format were designed using Autodesk Inventor software.

Table 1 displays the dimensional and geometric characteristics of the converging nozzle models evaluated in this topic.

Table 1. Dimensional and geometric characteristics of the converging nozzle models evaluated in this topic.

Nozzle Model	Shape	Feed Channels (mm)	
		D_{inlet}	D_{outlet}
Original	Spherical (Half sphere with a radius of 6.5 mm)	3.0	2.5
1	Conical (Diameter equal to 6.5 mm and height of 6.1 mm)	3.0	2.5
2	Cone trunk (Larger base radius 6.5 mm, smaller base radius 2.0 mm and height 8.0 mm)	3.0	2.5
3	Cone trunk (Larger base radius 6.5 mm, smaller base radius 2.0 mm and height 8.0 mm)	6.0	2.5

Based on the dimensions and geometric characteristics presented in Table 1, Figure 4 illustrates the CAD models used to study the optimization of the converging nozzle that directs the molten alloy to the interior of the mold.

After the nozzle optimization study, a porosity analysis was performed at the upper base, a region identified as critical during numerical simulation due to the presence of shrinkage porosities. In the porosity study, four riser models for shrinkage compensation were evaluated. Table 2 summarizes the dimensions used in the design of these riser models, and Figure 5 shows the compensation riser models used in this study.

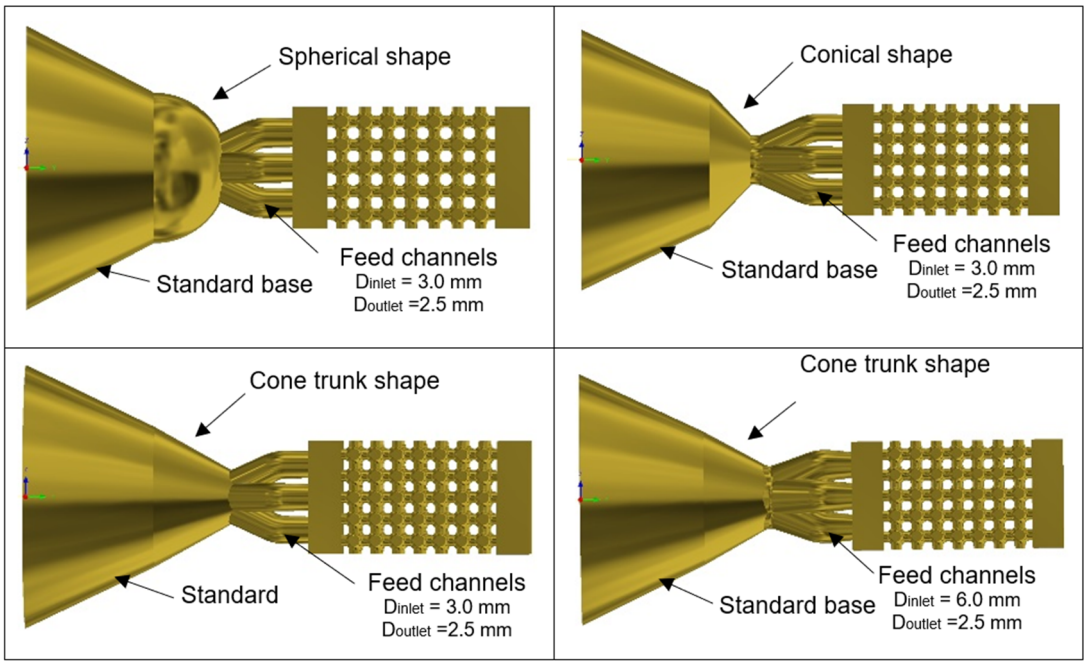


Figure 4. CAD models used to study the optimization of the converging nozzle which directs the molten alloy to the interior of the mold.

Table 2. Dimensions used in the design of the riser models for porosity compensation.

Riser Model	Dimension
1	Diameter of 6.0 mm and height of 2.0 mm
2	Diameter of 6.0 mm and height of 5.0 mm
3	Smaller diameter of 6.0 mm, larger diameter of 8.0 and height of 5 mm
4	Smaller diameter of 6.0 mm, larger diameter of 8.0 and height of 8.0 mm

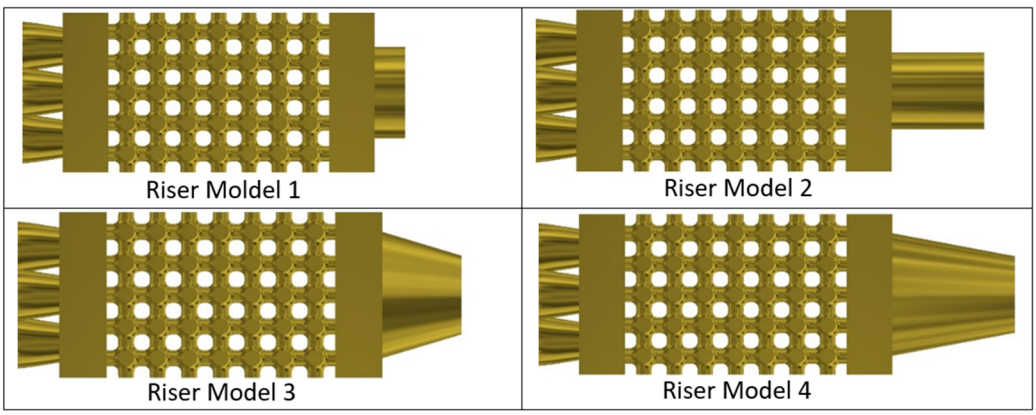


Figure 5. Compensation riser models designed for the study of shrinkage porosity.

In addition to the models shown in Figures 4 and 5, it was also necessary to model the crucible used for injection. This is because in simulations involving flow, the geometry of the domain in which the fluid will travel is essential to accurately represent the fluid dynamic phenomena. The external geometry of the crucible, which is complex and difficult to accurately measure, was digitized using Matter and Form Desktop 3D Scanner (Matter and Form Inc., Toronto, ON, Canada). The scanner emits two beams of red light that, when they fall on the surface of the object to be digitized, are detected by the equipment's camera and converted into points in a 3D coordinate system. The internal profile was obtained by a 3 mm offset using Autodesk Inventor (Version 2019, AutoDesk, San Francisco, CA, USA),

assuming that the thickness of the crucible is constant. Figure 6 shows the Matter and Form Desktop 3D Scanner performing the process of digitizing of the crucible geometry.

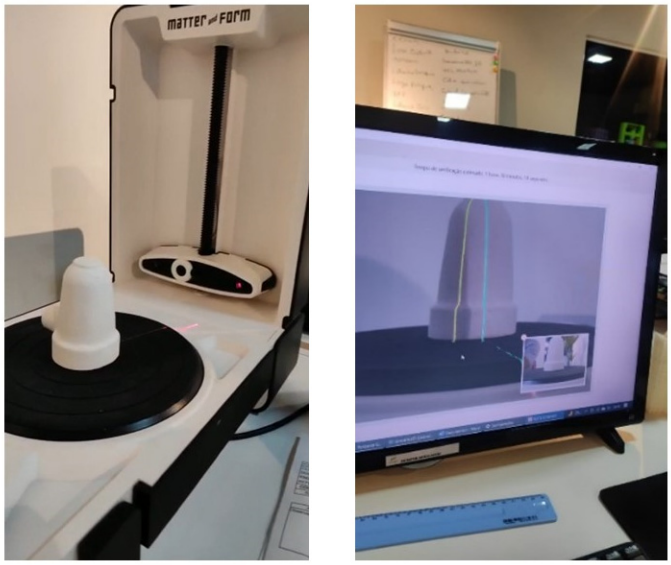


Figure 6. Matter and Form Desktop 3D Scanner performing the process of digitizing of the crucible geometry.

Having generated this external profile, it was possible to obtain the internal part with a roughing operation of 3 mm, using Autodesk Inventor. At this point, it was assumed that the thickness of the real crucible is constant. After producing the geometries in Autodesk Inventor, Visual-Mesh was used to discretize the study domain by generating a mesh composed of tetrahedral elements. The methodology sequence used in this work for domain discretization using Visual-Mesh:

I. Import the CAD geometry (using .igs file format);
II. Repair, if necessary, the geometry imported from Autodesk Inventor to ensure the geometry has a closed volume (using the Repair tool);
III. Create the mold with a cylinder geometry (Basic Shapes and Cylinder tools);
IV. Check for overlapping surface zones and create and merge volumes (Assembly tool);
V. Create 2D mesh, which will be the basis for the volumetric mesh (Surface Mesh tool);
VI. Check for the quality of the surface mesh and eliminate cracking, overlapping, intersection, poor-quality and coincident boundary nodes (Check Surface Mesh tool);
VII. Create 3D mesh using tetrahedral elements (Tetra Mesh tool).

The Figure 7 shows the mesh generated following the described methodology for one of the studied cases.

The alloy selected to develop this work was the Cu-7.90Al-5.40Mn alloy. The choice was made because it presents the SME both in the ingot and in the injected material, according to previously performed studies. The properties of the alloy required to feed the mathematical models were calculated using ProCAST via the right link to the CompuTherm database. The mold material chosen was Resincast plaster.

Visual-CAST is the environment used to impose the process conditions and feed the software the necessary information to properly perform the calculations. In this work, the method chosen to establish the process conditions was through the "Cast" tab, and the sequence used to model the casting processes:

I. Gravity Vector;
II. Volume Manager;
III. Interface HTC Manager;
IV. Process Condition Manager;
V. Simulate Parameters.

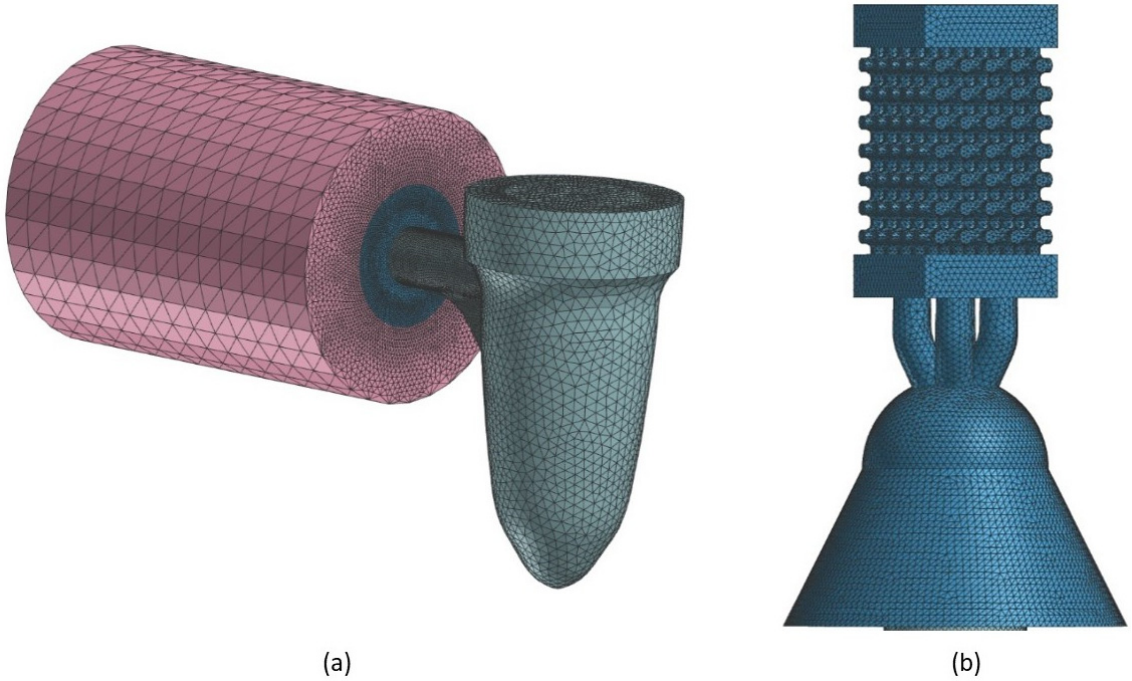


Figure 7. Mesh generated for analysis in the ProCAST software. (**a**) Complete set: mold, part and crucible. (**b**) Part mesh refinement.

In the Gravity Vector, the direction of gravity was defined. In the Volume Manager, the materials of each volume of the geometry are defined as well as their initial temperature and initial filling percentage. For the mold, the initial filling is considered 0%; for the crucible, a volumetric percentage compatible with the total mass needed to fill the part and the riser is used. In the HTC Manager Interface, the type of contact that the parts have can be selected. In this work, the COINC type contact was used for the contact between mold and metal, and for this contact, it is also necessary to define the heat transfer coefficient between the elements involved in the contact. Boundary conditions are created in the Process Condition Manager. In this work, for each case, thermal conditions of heat transfer, rotation geometry, fluid dynamics of wall pressure, etc., were imposed. Table 3 shows the summary of the input data used in this analysis.

Table 3. Values used in the design of the riser models.

Variable	Input Data
Cu-based SMA (%wt) SMA	Cu-7.90Al-5.40Mn
Mold	Resincast refractory plaster
Filling method	Centrifugal
Rotation speed (rpm)	400
Rotation time (s)	11
Superheat (°C)	5
Solidus temperature (°C)	993 (calculated using CompuTherm)
Liquidus temperature (°C)	1038 (calculated using CompuTherm)
Mold temperature (°C)	420 (constant)
Temperature outside the mold (°C)	Room temperature
Coefficient of heat exchange between the mold and the environment ($W/m^2 \cdot K$)	65 (forced convection)
Metal/mold interface heat transfer coefficient (hi in $W/m^2 \cdot K$)	535
Cast alloy mass (g)	25
Distance between mold inlet and center of rotation (mm)	120

Finally, the simulation parameters are imposed through the "Simulate Parameters" tool. For this work, we used a pre-definition for the centrifugal process; however, some parameters were changed to better suit our specific case.

The software also presents three basic tabs with simulation parameters (General, Thermal and Flow). In addition to these, in this work, we activated Turbulence model, choosing the Realizable k-epsilon model, as it has already been proven in several experiments that the realizable model k–ε provides better accuracy for flows involving rotations, strong recirculation or separation [54].

3. Mathematical Modeling

Applicable to any transport phenomenon, the governing equations for solidification modeling are the conservation of mass, conservation of momentum or momentum equation and energy equation [55].

The equation for conservation of mass, or continuity equation, used in ProCAST is given by [56–58]:

$$\frac{\partial \rho}{\partial t} + \nabla \cdot (\rho \vec{u}) = \mathbf{0} \tag{1}$$

where $\vec{u}$ the velocity, t is the time, ρ represents the density and the operator ∇, referred to as grad, nabla or del, represents the partial derivative of a quantity with respect to all directions in the chosen coordinate system.

The linear momentum equation, derived from the Navier–Stokes equations, used by ProCast is given by [57,58]:

$$\rho \frac{\partial u_i}{\partial t} + \rho u_j \frac{\partial u_i}{\partial x_j} + \frac{\partial}{\partial x_j}\left[p\delta_{ij}(\mu + \mu_T)\frac{\partial u_i}{\partial x_j}\right] = \rho g_i - \frac{\mu}{K}u_i \tag{2}$$

where p is the pressure, g_i the gravity acceleration, δ_{ij} the kronecker delta, μ the viscosity, μ_T the turbulent viscosity and K is the permeability, which reflects the resistance of the solid pattern to fluid flow, and is calculated using the Kozeny–Carmen equation [56].

$$K(g_s(t), \lambda_2(t)) = \frac{(1 - g_s(t))^3}{g_s(t)^2}\frac{{\lambda_2}^2(t)}{180} \tag{3}$$

where $g_s(t)$ is the solid volume fraction and $\lambda_2(t)$ is the secondary dendrite arm spacing, which can be evaluated at any point in the soft zone using a thickening law [46].

The ProCAST software uses four types of energy equation that are chosen depending on how heat flows through the metal and mold and how it is released to the environment. The methods are linear conduction transient, nonlinear conduction transient, transient laminar advection–diffusion and transient turbulent advection–diffusion. Linear conduction transient can be calculated by [57,58]:

$$\rho c_p \frac{\delta T}{\delta t} - \nabla[k\nabla T] - q(x) = 0 \tag{4}$$

where T represents the vectors of nodal temperatures, $q(x)$ the spatially variable volumetric heat source, ρ the constant density, c_p is the specific heat constant and k is the conductivity constant.

The nonlinear conduction transient can be calculated by the equation [57]:

$$\rho \frac{\delta H}{\delta T}\frac{\delta T}{\delta t} - \nabla[k\nabla T] - q(x) = 0 \tag{5}$$

in which case $\rho = \rho_o f(T)$ is the temperature-dependent density, $k = k_o f(T)$ is the temperature-dependent conductivity and H is the enthalpy as a function of temperature calculated by:

$$H(T) = \int_0^T c_p dT + L[1 - f_s(T)] \tag{6}$$

where L is the latent heat and fs is the solid volume fraction.

For transient laminar advection–diffusion, the used equation is [57]:

$$\rho \frac{\partial H}{\partial t} - \rho u_i \frac{\partial H}{\partial x_i} - \nabla(k \nabla T) - q = 0 \tag{7}$$

where $u_i = f_l u_{i,liq}$ is the surface velocity component, f_l is the liquid volume fraction and $u_{i,liq}$ is the current velocity of the liquid.

Finally, for transient turbulent advection–diffusion the equation used is [57]:

$$\rho \frac{\partial H}{\partial t} - \rho u_i \frac{\partial H}{\partial x_i} - \nabla \left[(k + \frac{\mu_T}{\sigma_T}) \nabla T \right] - q = 0 \tag{8}$$

where μ_T is the turbulent viscosity and σ_T is the turbulent Prandtl number.

The turbulent vortex viscosity is calculated from the turbulent kinetic energy, k_T, and the turbulent dissipation rate, ϵ, as follows:

$$\mu_T = \frac{C_\mu \rho k_T^2}{\epsilon} \tag{9}$$

where C_μ = 0.09 is a default value.

The conservation equation for turbulent kinetic energy used by the software is given by [46]:

$$\frac{\partial(\rho k_T)}{\partial t} + u_j \frac{\partial(\rho k_T)}{\partial x_j} - \frac{\partial}{\partial x_j} \left(\frac{\mu_T}{\sigma_k} \frac{\partial k_T}{\partial x_j} \right) = \mu_T G - \rho \epsilon \tag{10}$$

where:
$k_T = \frac{1}{2}(u^2 + v^2 + w^2)$;
u, v, w = fluctuating velocity components;
σ_k = Prandtl number of turbulent kinetic energy, typically set to 1;
$G = \left(\frac{\partial u_i}{\partial x_j} + \frac{\partial u_j}{\partial x_i} \right) \frac{\partial u_i}{\partial x_j}$ = turbulence generation rate;
ϵ = turbulence dissipation rate.

The turbulence dissipation rate used in Equation (10) can be calculated by:

$$\frac{\partial(\rho \epsilon)}{\partial t} + u_j \frac{\partial(\rho \epsilon)}{\partial x_j} - \frac{\partial}{\partial x_j} \left(\frac{\mu_T}{\sigma_\epsilon} \frac{\partial \epsilon}{\partial x_j} \right) = \frac{\epsilon}{k} (C_1 \mu_T G - C_2 \rho \epsilon) \tag{11}$$

where σ_ϵ is the Prandtl number for the turbulence dissipation rate, normally defined as 1.3, and the default constant values are C_1 = 1.44 and C_2 = 1.92.

The initial and boundary conditions for solving the previous equations are applied to temperature, velocity, pressure, fixed turbulent kinetic energy, fixed turbulent dissipation rate and specific, convective and radiation heat flux [58]. An iterative algorithm is used to simulate solidification by solving the equations of motion and energy, finding a coherent solution between the enthalpy and temperature results. More details on this strategy can be found in [56,59].

3.1. Turbulence Modeling

According to [56], ProCAST models turbulence using the Reynolds-averaged Navier–Stokes equations (RANS), where the additional turbulent stresses arising from the averaging procedure are approximated using the vortex viscosity approach. In this approximation,

the Reynolds stresses are assumed to be proportional to the mean rate of the strain tensor in an analogy to the laminar stress–strain relationship. The proportionality constant is called the turbulent viscosity μ_T.

There are several models in the literature to obtain turbulent viscosity. Popular among these are the two-equation turbulence models, in which two additional transport equations are solved for the kinetic energy of turbulence (k) and the rate of turbulence dissipation (ϵ). ProCAST has the following two-equation turbulence models [46]: Standard k–ε Model, RNG k–ε Model and Realizable k–ε (RKE).

As aforementioned, for flows involving rotations, strong recirculation or separation, it has been proven in several experiments that the realizable model k–ε provides better accuracy [54]. The standard k–ε model is based on the model proposed by Launder and Spalding [60].

The transport equations for k and ε are [54]:

$$\frac{\partial(\rho k)}{\partial t} + \frac{\partial(\rho u_j k)}{\partial x_j} = \rho P - \rho\varepsilon + \frac{\partial}{\partial x_j}\left[\left(\mu + \frac{\mu_T}{\sigma_k}\right)\frac{\partial k}{\partial x_j}\right] \tag{12}$$

$$\frac{\partial(\rho \varepsilon)}{\partial t} + \frac{\partial(\rho u_j \varepsilon)}{\partial x_j} = C_1 \frac{\varepsilon}{k}\rho P - C_2 \frac{\varepsilon}{k}\rho\varepsilon + \frac{\partial}{\partial x_j}\left[\left(\mu + \frac{\mu_T}{\sigma_\varepsilon}\right)\frac{\partial \varepsilon}{\partial x_j}\right] \tag{13}$$

with the turbulence production term P defined as:

$$P = \mu_T\left(\frac{\partial u_i}{\partial x_j} + \frac{\partial u_j}{\partial x_i} - \frac{2}{3}\frac{\partial u_m}{\partial x_m}\delta_{ij}\right) - \frac{2}{3}k\frac{\partial u_m}{\partial x_m} \tag{14}$$

The constants used in this model assume the following default values: $C_1 = 1.44$ e and $C_2 = 1.92$.

The realizable k–ε turbulence model (RKE) is described and characterized as a variant of the standard k–ε model. In particular, the RKE model can be distinguished from the standard k–ε model by the following [54]:

I. Replacing the transport equation for ε in the standard k–ε model with a similar transport equation that models the dissipation rate according to the dynamic behavior of the mean square vorticity fluctuation in the high turbulent Reynolds Number limit;
II. Replacing the eddy viscosity equation of the standard k–ε model with an eddy viscosity equation that ensures satisfaction of the realizability constraints (for the normal and shear turbulent stress components).

The transport equation for turbulent kinetic energy, k, in the RKE model remains unchanged from the standard k–ε model and the transport equation for ε, in the achievable RKE model, can be written as [54]:

$$\frac{\partial(\rho \varepsilon)}{\partial t} + \frac{\partial(\rho u_j \varepsilon)}{\partial x_j} = C_1\rho S\varepsilon - C_2\rho\frac{\varepsilon^2}{(k+\sqrt{\varepsilon})} + \frac{\partial}{\partial x_j}\left[\left(\mu + \frac{\mu_T}{\sigma_\varepsilon}\right)\frac{\partial \varepsilon}{\partial x_j}\right] \tag{15}$$

where: $C_1 = max\left[0, 43.\frac{\eta}{\eta+5}\right]$, $C_2 = 1.92$, $C_\mu = \frac{1}{A_0 + A_5 U^* \frac{k}{\varepsilon}}$, $\eta = S\frac{k}{\varepsilon}$, $S = \sqrt{2S_{ij}S_{ij}}$ and $U^* = \sqrt{\left(2S_{ij}S_{ij} + \widetilde{\Omega}_{ij}\widetilde{\Omega}_{ij}\right)}$, $\widetilde{\Omega}_{ij}$ is the average rate of rotation seen in a rotating frame with angular velocity ω_k. The parameter A_5 is determined by $A_5 = \sqrt{6}cos(\phi)$, $\phi = \frac{1}{3}arccos\left(\sqrt{6}W\right)$, $W = \frac{S_{ij}S_{jk}S_{ki}}{\widetilde{S}^3}$ and $\widetilde{S} = \sqrt{(S_{ij}S_{ij})}$. The value of A_0 is taken as 4.04.

3.2. Porosity Modeling

There are essentially two types of solidification porosity [54]:

- Shrink porosity: solidification shrinkage cannot be compensated by incoming liquid flow when feed flow is no longer possible. Consequently, shrinkage porosity is formed.
- Gas porosity: gas porosity is the result of two concomitant mechanisms among solidification, shrinkage and segregation of gases. The higher density of the solid induces a suction of the viscous liquid towards the pasty permeable zone, thus decreasing the pressure in the liquid. Being segregated in the remaining part of the liquid, the gas in the liquid can reach a concentration that exceeds the solubility limit, especially since this limit decreases with the temperature, and the pressure of the liquid. Nucleation and pore growth must be considered at this stage.

Two main equations are used to describe porosity formation during solidification [44]. The first governing equation is the conservation of alloy mass, which is a continuity equation. Assuming that the solid phase is not moving and that there is no deformation and, in addition, neglecting the specific mass of the bubbles, the average mass conservation equation written for both phases gives [56]:

$$\frac{\partial}{\partial t}[\rho_s g_s + \rho_l g_l] + \nabla(\rho_l g_l v_l) = 0 \tag{16}$$

where ρ_s is the specific mass of the solid and v_l is the effective velocity of the fluid among the solid cast (i.e., $v = g_l v_l$). If porosity formation has already occurred, the volume fraction of liquid, g_l, is given by [55].

$$g_l = 1 - g_s - g_p \tag{17}$$

g_s is the solid volume fraction and g_p is the pore volume fraction.

The continuity equation can also be written as [54]:

$$div(\rho_l g_l v_l) - \rho_l \frac{\partial g_p}{\partial t} = -\frac{\partial \langle \rho \rangle}{\partial T}\frac{\partial T}{\partial t} \tag{18}$$

where $\rho = (\rho_s \cdot g_s + \rho_l \cdot (1 - g_s))$ is the average mass of the solid–liquid mixture without porosity. Solidification shrinkage and specific mass variations, the term on the right side of the equation, can be compensated by interdendritic liquid feeding (first term on the left member) or by microporosity formation (second term on the left member) [54].

The other equation is the Darcy flow equation, which is a flow moment equation, that governs the resistance of a porous medium to the flow of viscous liquid. The porous medium is the solid dendritic network in which the alloy solidifies. The Darcy flow equation is [44]:

$$v = g_l v_l = -\frac{K}{\mu}[grad p_l - \rho_l g] \tag{19}$$

where p_l is the local pressure in the liquid, K is the permeability of the solid cast, μ is the dynamic viscosity of the liquid and g is the gravity vector. Most terms are alloy properties. Combining the continuity equations with Darcy flow:

$$div\left[\rho_l \frac{K}{\mu}(grad p_l - \rho_l g)\right] + \rho_l \frac{\partial g_p}{\partial t} = \frac{\partial \langle \rho \rangle}{\partial T}\frac{\partial T}{\partial t} \tag{20}$$

As it can be seen, two unknown scalar fields appear in this equation: the liquid pressure, $p_l(x,t)$, and the microporosity volume fraction, $g_p(x,t)$. The terms p_l and g_p are solved by applying boundary conditions.

4. Results and Discussion

4.1. Converging Nozzle Optimization: Simulation

Table 4 summarizes the fill time and nozzle recirculation results obtained in this analysis. The assessment of whether or not there was recirculation in the nozzle refers to the alloy that would be expelled from the mold when changing the flow direction during filling.

Table 4. Values used in the design of the nozzle models.

Evaluated Parameter	Nozzle Model			
	Original	Model 1	Model 2	Model 3
Filling time (s)	0.53	0.48	0.46	0.44
Recirculation in the converging nozzle	Yes	Yes	Yes	No
Shrinkage porosity (on the top base)	58.85%	61.18%	61.45%	62.62%

Observing the data presented in Table 4, the filling time improved by 17% and the recirculation of the alloy was eliminated in the simulation with nozzle model 3. This result was achieved by analyzing and identifying the defects present in the simulations with the original nozzle profile and afterwards implementing new profiles, similar to the methodology used by Kumar et al. [61].

In the simulations with the original profile, it was possible to identify that, under the applied injection conditions, the molten metal is directed first to the wall on the right side of the nozzle and, subsequently, flows to the center of the converging point of the feed channels that ultimately inject the alloy inside the mold. In the case of the original nozzle profile, due to the spherical curvature, a large part of the injected molten mass must perform a curved trajectory, changing the flow direction by almost 90°. This, consequently, leads a portion of the molten alloy on a tangent to the entrance of the feed channels and to the opposite wall, which ultimately changed the flow direction of the molten mass by 180°, generating recirculation.

In view of this analysis, it is clear that the recirculation is primarily explained by the lack of orientation provided by the geometry of the original nozzle, making it difficult for the alloy to reach the feed channels and wasting a large part of the centrifugal flow inertial energy. In order to overcome this problem, the nozzles designed in this work have a profile directed towards the converging point of the feed channels, reducing the direction changes in the molten flow. This result is supported by the reduction in filling time observed as the nozzle models were optimized. The second point that favored recirculation was the restriction generated by the small diameters of the feed channels. By increasing the feed channel inlet diameter from 3 mm to 6 mm, this problem was solved, generating a feed system without recirculation and with smaller filling time.

Figure 8 displays the filling time profile for each model. It can be seen that the original model has more regions with longer filling times, whereas models 2 and 3 show great improvements. It is also possible to infer that the upper base is the part of the piece that takes the longest to fill.

Figure 9 shows the recirculation in each model. The software presented a limitation when imposing an open boundary condition in the region where the alloy would be expelled to the environment due to the counterflow, so the representation of material loss due to recirculation is displayed as an alloy accumulation on the wall that, when colliding with the standard base wall, returns to the correct flow direction. In the real injection, the material is expelled out of the mold.

In the original model, the fluid begins to recirculate at 0.32 s but reaches a maximum counterflow at 0.38 s (Figure 9a); in model 1, the fluid recirculation starts at 0.30 s and peaks at 0.34 s (Figure 9b); model 2 exhibits a maximum recirculation at 0.35 s (Figure 9c); and model 3 has no recirculation (Figure 9d). From these images, we can infer that the nozzle model that presented the highest recirculation was the original model, and that the improvements made in the nozzle design had gradual positive effects until reaching the ideal model, which is model 3.

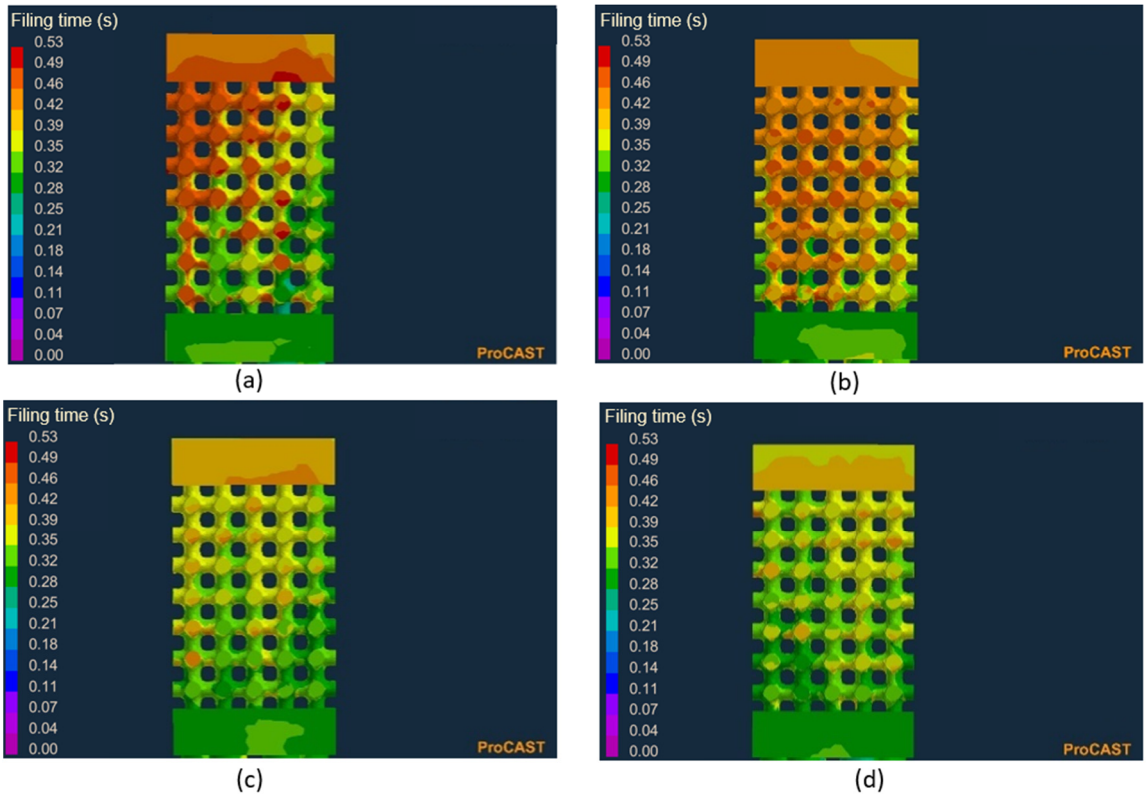


Figure 8. Color gradient for part filling time. (**a**) Original model. (**b**) Nozzle model 1. (**c**) Nozzle model 2. (**d**) Nozzle model 3.

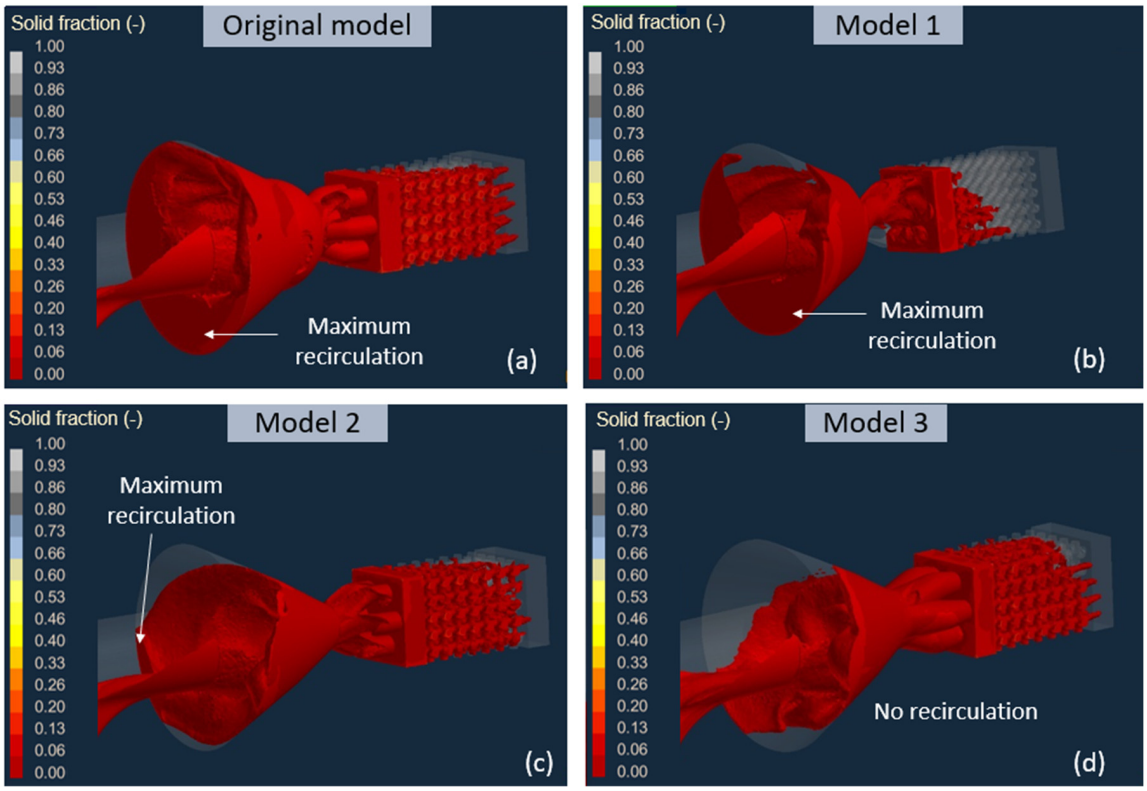


Figure 9. Maximum recirculation in each model (**a**) t = 0.38 s original profile, (**b**) t = 0.34 s modified profile with nozzle model 1, (**c**) t = 0.35 s modified profile with nozzle model 2 and (**d**) t = 0.34 s modified profile with nozzle model 3.

Another parameter affected by changing the filling nozzle construction parameters was the maximum gas pressure inside the mold. Figure 10 shows the points of maximum pressure of the gas inside the mold. The original model (Figure 10a) presented points with maximum pressure distributed in the center of the part, with a maximum value of 2.81 bar. Model 1 showed a similar behavior (Figure 10b), with a maximum pressure of 3.98 bar in one segment of the cell structure. Models 2 and 3 (Figure 10c,d) also presented maximum pressure points on the upper base of the part but compared to the previous models showed a reduction in maximum gas pressure, showing maximum pressure points of 2.24 and 2.06 bar, respectively.

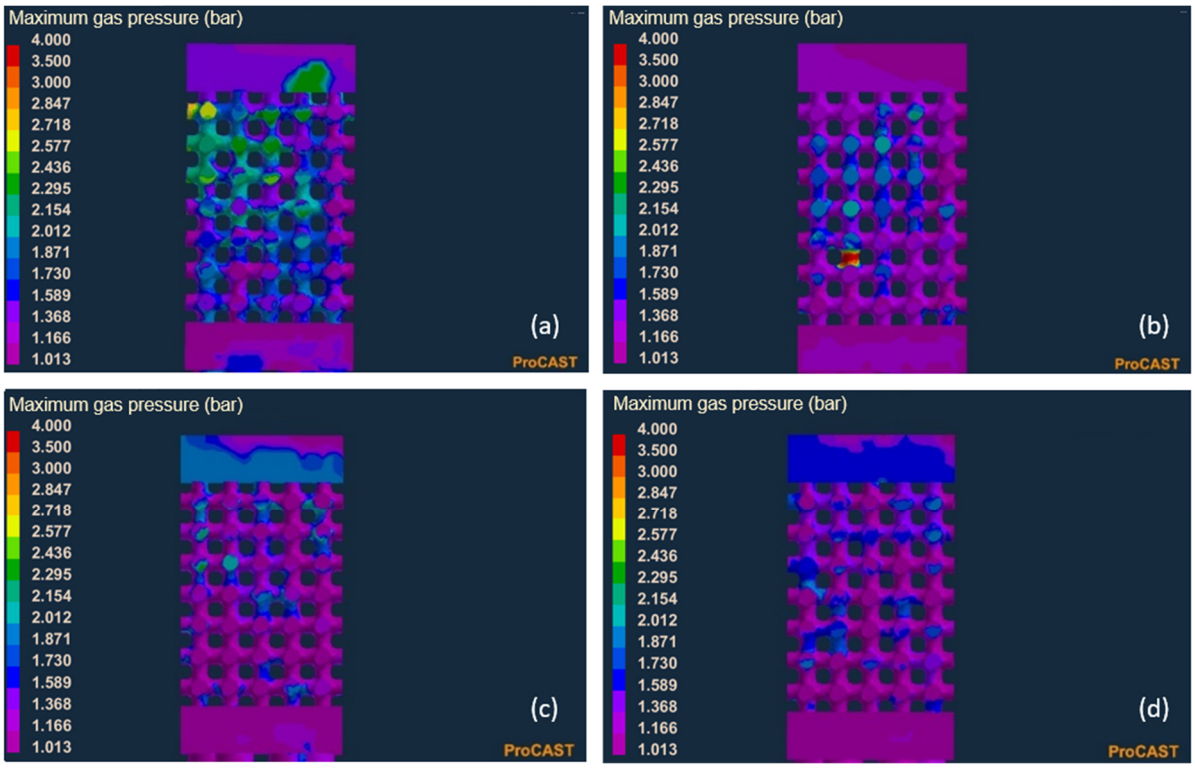


Figure 10. Maximum gas pressure inside the mold. (**a**) Original profile. (**b**) Modified profile 1. (**c**) Modified profile 2. (**d**) Modified profile 3.

The pressure variation observed in each case is due to gas entrapment. The results presented in Figure 10 show that the optimization of the feeding system, in addition to improving the flow of molten metal into the mold, has a positive influence on the removal of air from the mold, thus reducing the internal pressures of the mold and improving the filling of the part details in the mold.

In addition to the pressure of the trapped gas, the pressure of the alloy was also evaluated, and in this analysis, it was possible to verify that the pressure of the alloy becomes higher at points far from the inlet gate, probably due to the effect of the centrifugal force that takes into account the distance from the rotation axis. This pressure increase in the outermost segments can cause the mold to rupture, consequently leading to filling failures. Figure 11 shows an example of the pressure gradient of the alloy in the mold. The gradient displayed was generated in the simulations of model 3, but all evaluated cases show a similar behavior.

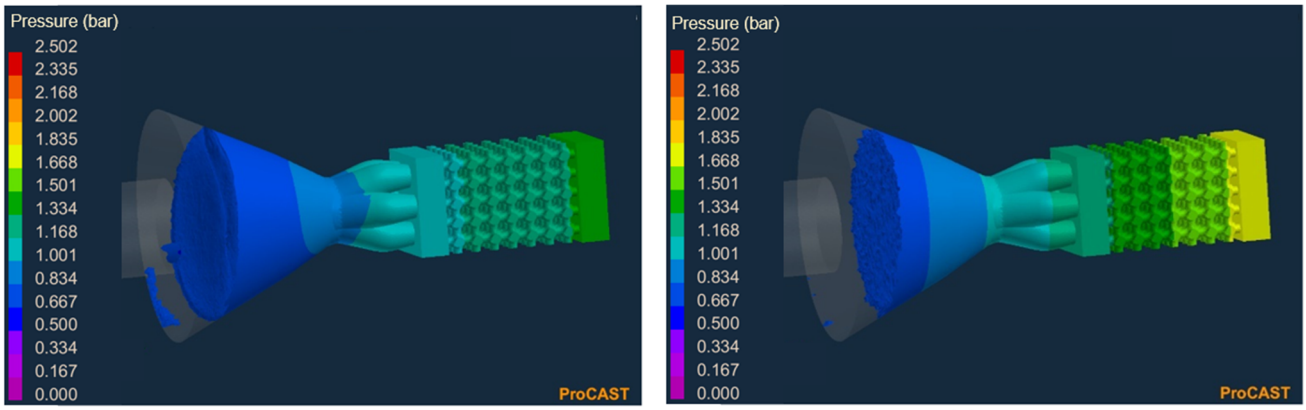


Figure 11. Alloy pressure inside the mold. (**a**) Nozzle model 3 at 0.44 s. (**b**) Nozzle model 3 at 0.71 s time.

Regarding the misrun sensitivity, Figure 12 compares the risk that each nozzle model generates. Misrun sensitivity is a measure used by the ProCAST software to assess the probability of occurrence of filling failures in a casting process. Taking into account factors such as mold geometry, material properties and operating conditions, it indicates the ability of the injection system to correctly fill all regions of the mold, ensuring proper formation of the casting. We can notice that the original model is the one that presents more points with a high risk of filling failures and, as the geometries were being optimized, the number of points of high risk decreased.

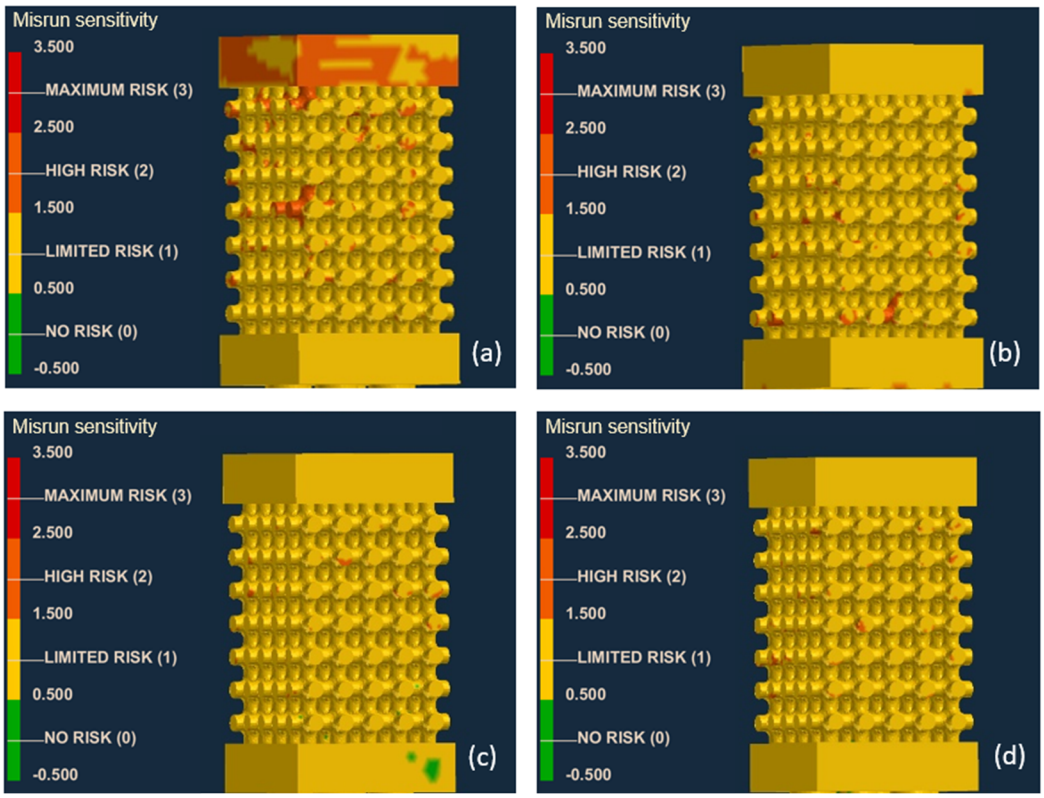


Figure 12. Misrun sensitivity. (**a**) Original profile. (**b**) Nozzle model 1. (**c**) Nozzle model profile 2. (**d**) Nozzle model 3.

This occurs because, as shown in the previous analyses, the nozzle models with high levels of recirculation also have higher internal gas pressures and reduced flow inertia,

which hinders the filling of the part details in the mold. In addition to the internal pressure of the gas and pressure drop, another point that must be considered is that the recirculation reduces the temperature at which the alloy comes into contact with the mold, decreasing its viscosity and consequently its castability.

4.2. Converging Nozzle Optimization: Experiments

The image in Figure 13 shows the comparison between the real parts injected with the original feeding system (Figure 13a) with the designed model 3 feeding system (Figure 13b). Both pieces showed signs of cracking in the casting as some regions that should have been empty close to the upper base were filled. A hypothesis for this problem was discussed in the analysis of the virtual prototyping and presented in Figure 11. In this discussion, it was identified that the most distant points from the feed channels presented the highest pressures, and this could harm the structure of the mold.

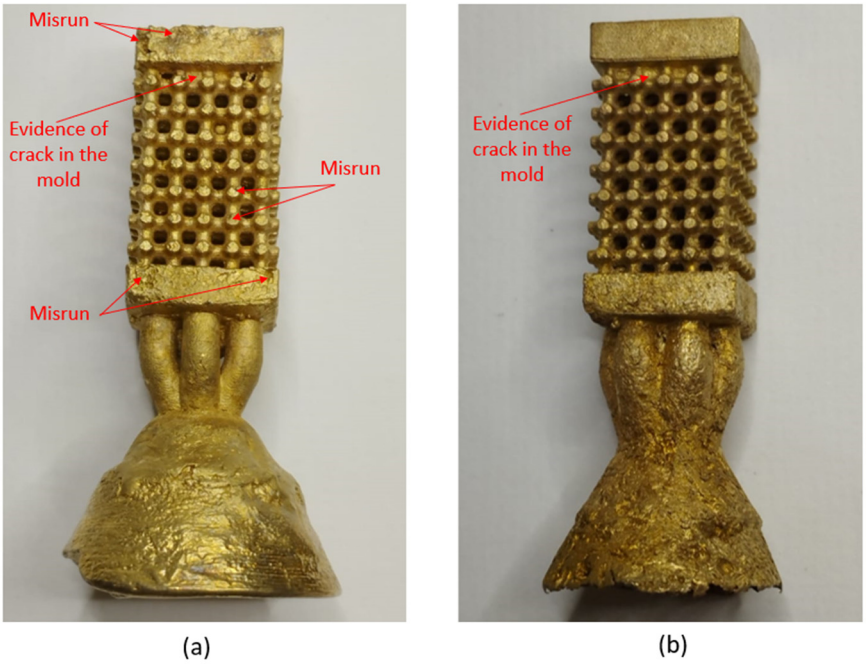


Figure 13. Photo of the parts injected with the feeding systems. (**a**) Original. (**b**) Modified model 3.

The part injected with the original feeding model (Figure 13a) shows regions with filling defects in the upper base, mainly in the left corner and in the lower base, but with weaker intensity. These experimental results are similar to the results presented in the virtual prototyping shown in Figure 12, which indicate high risks of filling failure in several regions in the upper base and some points of the cell structure. The numerical simulation did not predict, however, the risk of filling failure in the lower base, which was observed in the experimentally cast part. On the other hand, the real component manufactured with the nozzle model 3 showed an improvement in relation to the filling of the details of the part since its structure did not show a lack of filling. As shown in Figure 12d, these results were pointed out in the simulation results as the software signaled high risks of filling failure in a few internal elements of the cellular structure and limited risk in the rest of the piece.

In addition to the filling improvement, it was possible to identify in the injection experiments that recirculation was eliminated in the designed nozzle model 3. As shown in Figure 3, when injecting the alloy with the original feeding model, the tip of the crucible was damaged during the process as the alloy recirculated and joined the piece with the crucible. As a result of this joining, the riser of the injected part with the original model presents a mark of the shape of the diameter of the crucible tip, as can be seen in Figure 14a.

In Figure 14b, however, we can see that this mark is not present, confirming that the recirculation was indeed reduced with the optimized model 3.



Figure 14. Signs of recirculation in the riser of the pieces. (**a**) Original. (**b**) Modified model 3.

4.3. Shrinkage Porosity Simulation

As shown in Table 4, all studied models in the nozzle optimization showed shrinkage porosity in the upper base, including the model with the best filling results (nozzle model 3). Model 3 presented shrinkage porosity in the upper base with a maximum of 62.62%. Observing these results, it is clear that the upper base is a critical point concerning porosity defects. It can also be noted that as the injection systems were optimized, the percentage of shrinkage porosity was high. This is because the optimization of the feed models allows a faster filling and consequently a greater thermal load to be dissipated during solidification inside the mold. This favors the formation of contraction porosities in the upper base, which does not present any compensation mechanism and is one of the last regions to solidify.

Figure 15 shows the position and a sectional view that shows the maximum shrinkage points in the virtually molded part with the optimized nozzle.

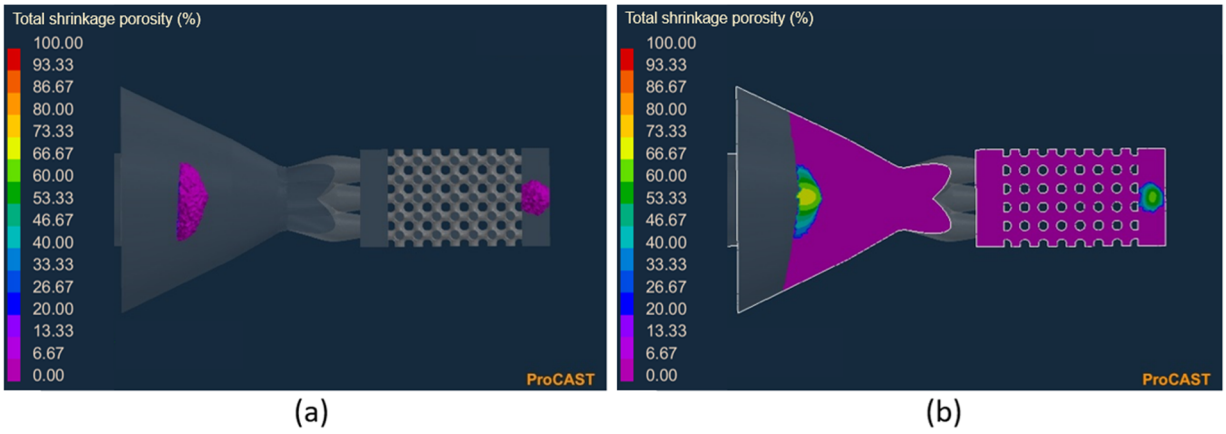


Figure 15. Shrinkage porosity in the original model with optimized converging nozzle. (**a**) Position of porosities. (**b**) Section showing region of maximum porosity.

According to Rajkolhe and Khan [62] and Ingle and Sorte [63], shrinkage defects such as porosity-considered closed shrinkage defects occur when there feed metal supply is insufficient to compensate for shrinkage as the metal solidifies.

This type of porosity can be reduced or eliminated with geometric modifications such as changes in the feeding system, insertion of mass to compensate for shrinkage, modification of the part geometry and with manipulation of injection parameters such as rotation speed, injection pressure and temperature, thermal insulation, among others. The focus of this work, however, was not to modify the injection parameters, mainly because the data used as boundary condition and input parameters were replicated from preliminary physical experiments. Therefore, in order to reduce the porosity in the part, compensation volumes were added and were designed to move the porosity to its interior. These volumes were positioned on the upper base and centered around the region identified as being the most critical concerning the presence of shrinkage porosity. All porosity cases evaluated in this topic were made from the optimized convergent nozzle model (nozzle model 3).

Figures 16–19 show the results obtained for each type of projected compensation volume. In riser models 1 and 2, the shrinkage compensation volume has the shape of a cylinder. In Figure 16, we can see that the riser model 1 displaced the porosity to its interior, but a large part is still present in the part because the volume does not have enough mass to compensate for the shrinkage of the alloy nor to change the temperature field in that region. In model 2, the height of the volume was increased by 3 mm in order to increase the compression mass. As it can be seen in Figure 17, it caused a greater displacement of porosity compared to the riser model 1, but a part of the porosity is still present in the cell structure.

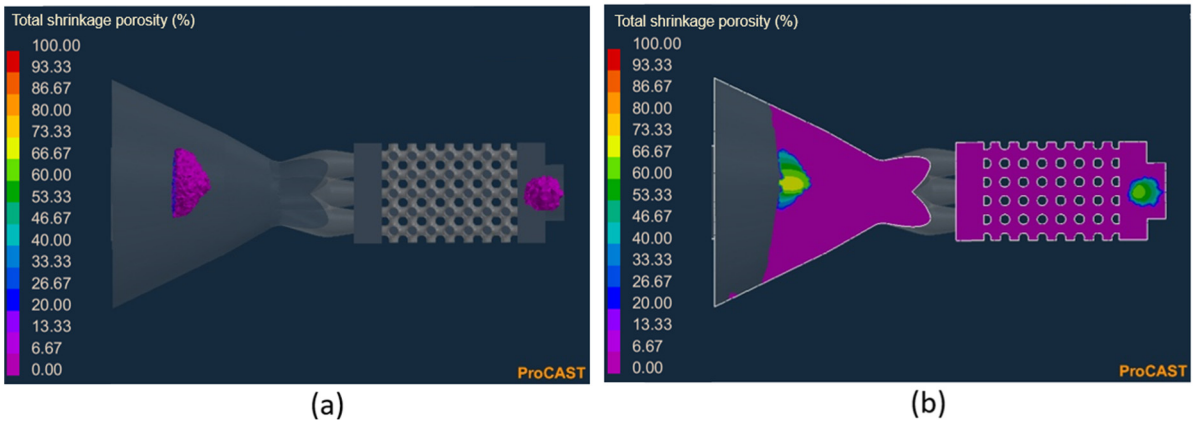


Figure 16. Shrinkage porosity riser model 1 with optimized converging nozzle. (**a**) Position of porosities. (**b**) Section showing region of maximum porosity.

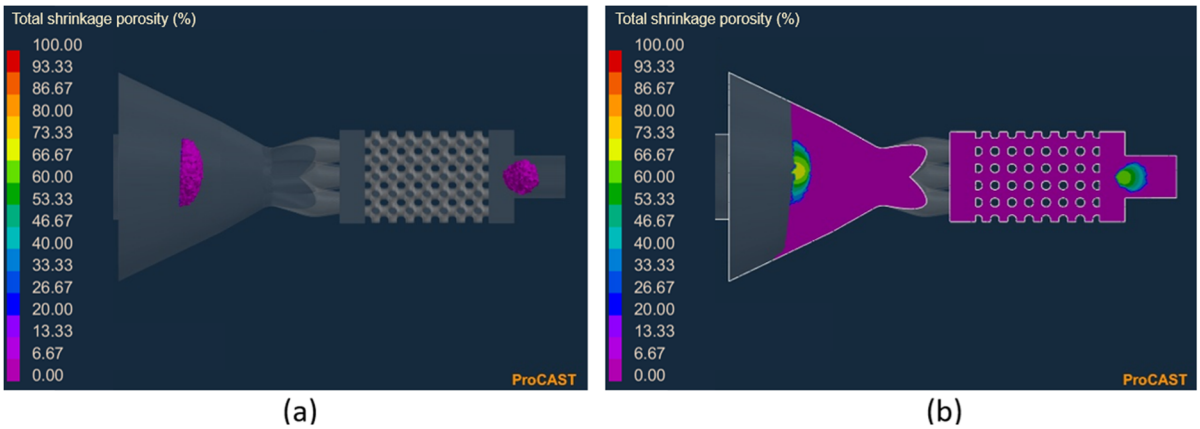


Figure 17. Shrinkage porosity riser model 2 with optimized converging nozzle. (**a**) Position of porosities. (**b**) Section showing region of maximum porosity.

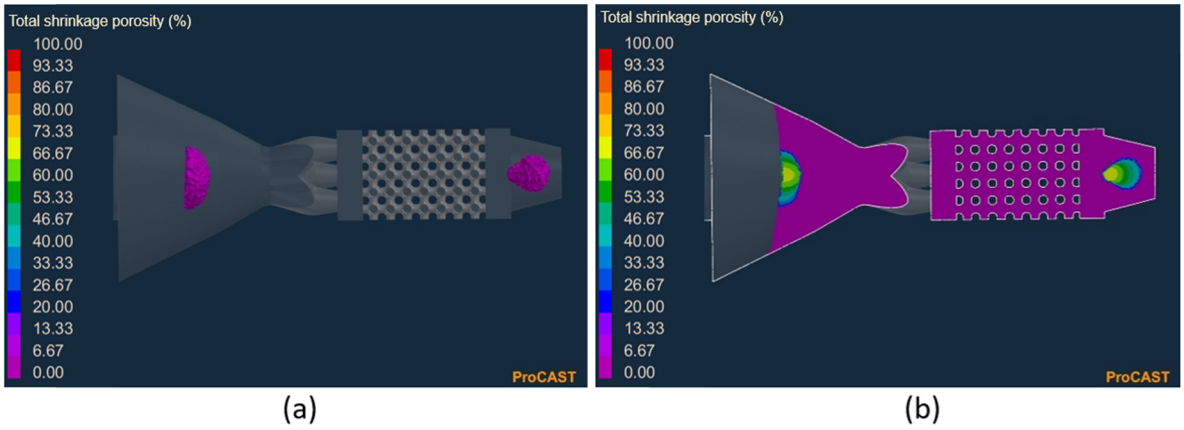


Figure 18. Shrinkage porosity riser model 3 with optimized converging nozzle. (**a**) Position of porosities. (**b**) Section showing region of maximum porosity.

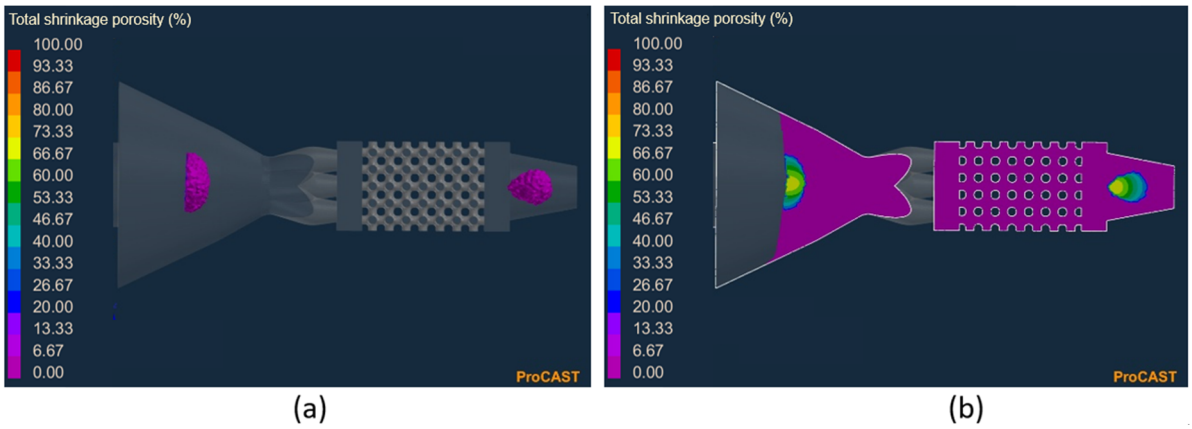


Figure 19. Shrinkage porosity riser model 4 with optimized converging nozzle. (**a**) Position of porosities. (**b**) Section showing region of maximum porosity.

The riser models 3 and 4 have volumes in the shape of a truncated cone (Figure 5). Model 3 generated a displacement that almost removed all the porosity of the upper region of the part (Figure 18). Based on this result, the riser model 4 was designed with the same diameter dimensions but with a greater height in relation to model 3, approximately 3 mm. In the case of the riser model 4, the displacement generated by the compensation volume was sufficient to completely displace the porosities to its interior, leaving the part free of shrinkage porosities, as can be seen in Figure 19.

5. Conclusions

In this work, virtual prototyping is used to optimize the efficiency and accuracy of a non-traditional precision casting process that uses centrifugal force to inject the molten alloy into the mold. This modified casting differs from traditional processes because it uses centrifugal force in the perpendicular direction to the rotation axis to inject the molten metal inside the mold; while traditional processes use centrifugal force in the same direction of the rotation axis.

The virtual castings carried out in this work enabled the analysis and design of the feeding systems for the production of a simple-cubic cellular structure with complex geometry manufactured with a copper-based shape memory alloy. The numerical simulation of the process allowed reducing and correcting possible defects that may impair the production and integrity of the part, especially recirculation and shrinkage porosity that mechanically weaken the component.

The results showed that gas circulation inside the mold has a strong influence on the filling process. Badly designed feeding systems tend to make it difficult for the gas to return and generate high pressures that can trap the gases, forming voids in the parts or causing damage such as cracking and mold rupture. Regarding the design of the studied part in this article, it is possible to conclude that the convergent nozzle proposed in model 3 is a better design to reduce filling time and eliminate recirculation, but due to the presence of retraction pores, it is necessary to add compensation for volume shrinkage. The shrinkage compensation volume that presented the best results has the shape of a truncated cone with a larger diameter of 8 mm, a smaller diameter of 6 mm and a height of 8 mm, such as the riser proposed in model 4 in this work.

Author Contributions: Conceptualization, C.E.S.A. and C.J.D.A.; methodology, C.E.S.A. and P.C.S.S.; software, C.E.S.A.; validation, C.E.S.A., C.J.D.A. and A.G.B.L.; formal analysis, C.E.S.A.; investigation, C.J.D.A. and P.C.S.S.; resources, C.J.D.A. and A.G.B.L.; writing—original draft preparation, C.E.S.A.; writing—review and editing, E.N.D.G. and J.M.P.Q.D.; visualization, E.N.D.G.; supervision, C.J.D.A. and A.G.B.L.; project administration, C.J.D.A.; funding acquisition, J.M.P.Q.D., C.J.D.A. and A.G.B.L. All authors have read and agreed to the published version of the manuscript.

Funding: This research was funded by Brazilian National Council for Scientific and Technological Development (CNPq) for the scholarship PQ-1C, grant number 302740/2018-0; the Paraíba State Research Support Foundation (FAPESQ-PB) for the project NISMArt, grant number 044/2023; and the Brazilian Coordination for the Improvement of Higher Education Personnel (CAPES) for the doctoral scholarship to Paulo César Sales da Silva and for the post-doctoral scholarship to Estephanie Nobre Dantas Grassi. In addition, this work is a result of the project "BlueWoodenHouse", with the reference POCI-01-0247-FEDER-047157, co-funded by the European Regional Development Fund (ERDF) through the Operational Programme for Competitiveness and Internationalization (COMPETE 2020), under the Portugal 2020 Partnership Agreement, and the project "BlueHouseSim", with reference 2022.06841.PTDC, funded by national funds (PIDDAC) through FCT/MCTES. Furthermore, this work was financially supported by Base Funding-UIDB/04708/2020 and Programmatic Funding-UIDP/04708/2020 of the CONSTRUCT-Instituto de I&D em Estruturas e Construções-funded by national funds through the FCT/MCTES (PIDDAC); and by FCT—Fundação para a Ciência e a Tecnologia through the individual Scientific Employment Stimulus 2020.00828.CEECIND.

Data Availability Statement: Not applicable.

Acknowledgments: The authors acknowledge the authors cited in the text that helped in the improvement of this paper as well as the ESI Group for granting the license for the ProCAST program (Ref: CA/ARDS/RSD_2007_01BR).

Conflicts of Interest: The authors declare no conflict of interest.

References

1. Mohammad, J.A.; Amirhesam, A.; Zohreh, S.; Narges, S.M.; Reza, M.; Haluk, K.; Mohammad, E. Shape memory response of cellular lattice structures: Unit cell finite element prediction. *Mech. Mater.* **2018**, *125*, 26–34. [CrossRef]
2. Zhang, Y.; Wang, P.; Xia, Y.; Zhou, P.; Xie, Y.; Xu, S.; Zhang, C. Application of a Shape-Memory Alloy Concentrator in Displaced Patella Fractures: Technique and LongTerm Results. *J. Knee Surg.* **2016**, *30*, 166–173. [CrossRef]
3. Gibson, L.J.; Ashby, M.F. *Cellular Solids-Structure and Properties*; Cambridge University Press: Cambridge, UK, 1997. [CrossRef]
4. Ju, J.; Summers, J.D.; Ziegert, J.; Fadel, G. Design of Honeycombs for Modulus and Yield Strain in Shear. *Trans. ASME J. Eng. Mater. Technol.* **2012**, *134*, 11–22. [CrossRef]
5. Tan, H.; Qu, S. Impact of Cellular Materials. In *Cellular and Porous Materials in Structures and Processes*; Altenbach, H., Öchsner, A., Eds.; CISM International Centre for Mechanical Sciences: Udine, Italy; Springer: Vienna, Austria, 2010; Volume 521. [CrossRef]
6. Smith, M.; Guan, Z.; Cantwell, W.J. Finite element modelling of the compressive response of lattice structures manufactured using the selective laser melting technique. *Int. J. Mech. Sci.* **2013**, *67*, 28–41. [CrossRef]
7. Yan, C.; Hao, L.; Hussein, A.; Young, P.; Raymont, D. Advanced lightweight 316L stainless steel cellular lattice structures fabricated via selective laser melting. *Mater. Des.* **2014**, *55*, 533–541. [CrossRef]
8. Karamooz Ravari, M.R.; Kadkhodaei, M. A computationally efficient modeling approach for predicting mechanical behavior of cellular lattice structures. *J. Mater. Eng. Perform.* **2015**, *24*, 245–252. [CrossRef]
9. Deshpande, V.S.; Fleck, N.A.; Ashby, M.F. Effective properties of the octet-truss lattice material. *J. Mech. Phys. Solids* **2001**, *49*, 1747–1769. [CrossRef]

10. Zhou, J.; Shrotriya, P.; Soboyejo, W. On the deformation of aluminum lattice block structures: From struts to structures. *Mech. Mater.* **2004**, *36*, 723–737. [CrossRef]
11. Labeas, G.; Sunaric, M. Investigation on the static response and failure process of metallic open lattice cellular structures. *Strain* **2010**, *46*, 195–204. [CrossRef]
12. Hao, L.; Seaman, O.; Felstead, M. Selective laser melting of a stainless steel and hydroxyapatite composite for loadbearing implant development. *J. Mater. Process. Technol.* **2009**, *209*, 5793–5801. [CrossRef]
13. McKown, S.; Shen, Y.; Brookes, W.K.; Sutcliffe, C.J.; Cantwell, W.J.; Langdon, G.S.; Nurick, G.N.; Theobald, M.D. The quasi-static and blast loading response of lattice structures. *Int. J. Impact Eng.* **2008**, *35*, 795–810. [CrossRef]
14. Rao, A.; Srinivasa, A.R.; Reddy, J.N. *Design of Shape Memory Alloy (SMA) Actuators*; Springer: New York, NY, USA, 2015.
15. Peairs, D.M.; Park, G.; Inman, D.J. Practical issues of activating self-repairing bolted joints. *LMFrt Mater. Struct.* **2004**, *13*, 1414–1423. [CrossRef]
16. Elahinia, M.; Moghaddam, S.N.; Andani, M.T.; Amerinatanzi, A.; Bimber, B.A.; Hamilton, R.F. Fabrication of NiTi through additive manufacturing: A review. *Prog. Mater. Sci.* **2016**, *83*, 630–663. [CrossRef]
17. Hadi, A.; Elahinia, M.; Qasemi, M.; Shayesteh Moghaddam, N. Modeling and Experiment of a Flexible Module Actuated by Shape Memory Alloy Wire. In Proceedings of the ASME 2014 Conference on Smart Materials, Adaptive Structures and Intelligent Systems, SMASIS 2014, Newport, RI, USA, 8–10 September 2014. [CrossRef]
18. Hadi, A.; Alipour, K.l.; Kazeminasab, S.; Amerinatanzi, A.; Elahinia, M. *Design and Prototyping of a Wearable Assistive Tool for Hand Rehabilitation Using Shape Memory Alloys*; American Society of Mechanical Engineers: New York, NY, USA, 2016. [CrossRef]
19. Amerinatanzi, A.; Shayesteh Moghaddam, N.; Ibrahim, H.; Elahinia, M. *Evaluating a NiTi Implant Under Realistic Loads: A Simulation Study*; American Society of Mechanical Engineers: New York, NY, USA, 2016. [CrossRef]
20. Moghaddam, N.S.; Skoracki, R.; Miller, M.; Elahinia, M.; Dean, D. Three Dimensional Printing of Stiffness-tuned, Nitinol Skeletal Fixation Hardware with an Example of Mandibular Segmental Defect Repair. *Procedia CIRP* **2016**, *49*, 45–50. [CrossRef]
21. Banhart, J. Manufacture, characterisation and application of cellular metals and metal foams. *Prog. Mater. Sci.* **2001**, *46*, 559–632. [CrossRef]
22. Mun, J.; Busse, M.; Thurman, J. Multilevel Metal Flow-Fill Analysis of Centrifugal Casting for Indirect Additive Manufacturing of Lattice Structures. In Proceedings of the ASME 2015 International Mechanical Engineering Congress and Exposition, Houston, TX, USA, 15–18 November 2015; Volume 2A: Advanced Manufacturing 2015. [CrossRef]
23. Oliveira, J.P.; Lalonde, A.D.; Ma, J. Processing parameters in laser powder bed fusion metal additive manufacturing. *Mater. Des.* **2020**, *193*, 108762. [CrossRef]
24. West, B.M.; Capps, N.E.; Urban, J.S.; Pribe, J.D.; Hartwig, T.J.; Lunn, T.D.; Brown, B.; Bristow, D.A.; Landers, R.G.; Kinzel, E.C. Modal analysis of metal additive manufactured parts. *Manuf. Lett.* **2017**, *13*, 30–33. [CrossRef]
25. Kok, Y.; Tan, X.P.; Wang, P.; Nai, M.L.S.; Loh, N.H.; Liu, E.; Tor, S.B. Anisotropy and heterogeneity of microstructure and mechanical properties in metal additive manufacturing: A critical review. *Mater. Des.* **2018**, *139*, 565–586. [CrossRef]
26. Shim, D.S.; Seo, J.Y.; Yoon, H.S.; Lee, K.Y.; Oh, W.J. Additive manufacturing of porous metals using laser melting of Ti6Al4V powder with a foaming agent. *Mater. Res. Express* **2018**, *5*, 86518. [CrossRef]
27. Dressler, A.D.; Jost, E.W.; Miers, J.C. Moore DG, Seepersad CC, Boyce BL (2019) Heterogeneities dominate mechanical performance of additively manufactured metal lattice struts. *Addit. Manuf.* **2019**, *28*, 692–703. [CrossRef]
28. Santo, L.S.; Gupta, S.K.; Bruck, H.A. Simulation of buckling of internal features during selective laser sintering of metals. *Addit. Manuf.* **2018**, *23*, 235–245. [CrossRef]
29. Li, X.; Tan, W. Numerical investigation of effects of nucleation mechanisms on grain structure in metal additive manufacturing. *Comput. Mater. Sci.* **2018**, *153*, 159–169. [CrossRef]
30. Demir, A.G. Micro laser metal wire deposition for additive manufacturing of thin-walled structures. *Opt. Lasers Eng.* **2018**, *100*, 9–17. [CrossRef]
31. McGregor, D.J.; Tawfick, S.; King, W.P. Automated metrology and geometric analysis of additively manufactured lattice structures. *Addit. Manuf.* **2019**, *28*, 535–545. [CrossRef]
32. Herzog, D.; Seyda, V.; Wycisk, E.; Emmelmann, C. Additive manufacturing of metals. *Acta Mater.* **2016**, *117*, 371–392. [CrossRef]
33. Zinovieva, O.; Zinoviev, A.; Ploshikhin, V. Three-dimensional modeling of the microstructure evolution during metal additive manufacturing. *Comput. Mater. Sci.* **2018**, *141*, 207–220. [CrossRef]
34. Carneiro, V.H.; Puga, H.; Meireles, J. Heat treatment as a route to tailor the yield-damping properties in A356 alloys. *Mater. Sci. Eng. A* **2018**, *729*, 1–8. [CrossRef]
35. Carneiro, V.H.; Puga, H. Solution Treatment Enhances Both Static and Damping Properties of Al–Si–Mg alloys. *Metall. Mater. Trans. A* **2018**, *49*, 5942–5945. [CrossRef]
36. Puga, H.; Carneiro, V.H.; Barbosa, J. Effect of grain and secondary phase morphologies in the mechanical and damping behavior of Al7075 alloys. *Met. Mater.* **2016**, *22*, 863–871. [CrossRef]
37. Tang, Y.; Tan, W.K.; Fuh, J.Y.H.; Loh, H.T.; Wong, Y.S.; Thian, S.C.H.; Lu, L. Micro-mould fabrication for a micro-gear via vacuum casting. *J. Mater. Process. Technol.* **2007**, *192–193*, 334–339. [CrossRef]
38. Xue, Y.; Wang, W.; Han, F. Enhanced compressive mechanical properties of aluminum based auxetic lattice structures filled with polymers. *Compos. Part B Eng.* **2019**, *171*, 83–191. [CrossRef]
39. Guo, J.; Samonds, M. Modeling of alloy casting solidification. *JOM* **2011**, *63*, 19–28. [CrossRef]

40. Horr, A.M.; Kronsteiner, J. On Numerical Simulation of Casting in New Foundries: Dynamic Process Simulations. *Metals* **2020**, *10*, 886. [CrossRef]
41. Papanikolaou, M.; Pagone, E.; Jolly, M.; Salonitis, K. Numerical Simulation and Evaluation of Campbell Running and Gating Systems. *Metals* **2020**, *10*, 68. [CrossRef]
42. Scampone, G.; Pirovano, R.; Mascetti, S.; Timelli, G. Experimental and numerical investigations of oxide-related defects in Al alloy gravity die castings. *Int. J. Adv. Manuf. Technol.* **2021**, *117*, 1765–1780. [CrossRef]
43. Chu, H.; Ping, J.; Shaoning, G.; Song, G.; Gaoyang, M.; Chunming, W. Multiphase-field simulation of grain coalescence behavior and its effects on solidification cracking susceptibility during welding of Al-Cu alloys. *Mater. Des.* **2021**, *211*, 110146. [CrossRef]
44. Mark, J.; Laurens, K. Modelling of defects in aluminium cast products. *Prog. Mater. Sci.* **2022**, *123*, 100824. [CrossRef]
45. Santamaría, J.A.; Sertucha, J.; Redondo, A.; Lizarralde, I.; Ochoa de Zabalegui, E.; Rodríguez, P. Towards the Prediction of Tensile Properties in Automotive Cast Parts Manufactured by LPDC with the A356.2 Alloy. *Metals* **2022**, *12*, 656. [CrossRef]
46. Xuan, M.; Chen, M. Optimal Design of the Submerged Entry Nozzle for Thin Slab Continuous Casting Molds. *Metals* **2021**, *11*, 1223. [CrossRef]
47. Zheng, H.; Zhang, Z.; Bai, Y. Numerical Simulation and Experimental Study on Compound Casting of Layered Aluminum Matrix Composite Brake Drum. *Materials* **2021**, *14*, 1412. [CrossRef]
48. Qiang, L.; Peng, G.; Guangxuan, L.; Yang, S.; Wenhui, Y.; Jianping, G.; Xian, L. Simulation Study on the Investment Casting Process of a Low-Cost Titanium Alloy Gearbox based on ProCAST. *Adv. Mater. Sci. Eng.* **2022**, *2022*, 4484762. [CrossRef]
49. Silva, R.; Madureira, R.; Silva, J.; Soares, R.; Reis, A.; Neto, R.; Viana, F.; Emadinia, O.; Silva, R. Numerical Simulation and Defect Identification in the Casting of Co-Cr Alloy. *Metals* **2022**, *12*, 351. [CrossRef]
50. Tan, R.; Liu, W.; Song, B.; Yang, S.-F.; Chen, Y.-F.; Zuo, X.-T.; Huang, Y. Numerical simulation on solidification behavior and structure of 38CrMoAl large round bloom using CAFE model. *J. Iron Steel Res. Int.* **2023**. [CrossRef]
51. You, L.; Yao, L.; Li, X.; Jia, G.; Lv, G. Numerical simulation and casting process optimization of cast steel node. *Int. J. Adv. Manuf. Technol.* **2023**, *126*, 5215–5225. [CrossRef]
52. Albuquerque, C.E.S.; Grassi, E.N.D.; Araújo, C.J. Castability of Cu-Al-Mn shape memory alloy in a rapid investment asting process: Computational and experimental analysis. *Int. J. Adv. Manuf. Technol.* 2023, *in press*. [CrossRef]
53. Simões, J.B.; Araújo, C.J. Nickel–titanium shape memory alloy mechanical components produced by investment casting. *J. Intell. Mater. Syst. Struct.* **2018**, *29*, 3748–3757. [CrossRef]
54. ESI. *ProCast Casting Simulation Suite*; ESI Software: Rungis, France, 2019.
55. Guo, Z.; Saunders, N.; Miodownik, A.P.; Schillé, J.-P.H. Modelling of materials properties and behaviour critical to casting simulation. *Mater. Sci. Eng. A* **2011**, *413–414*, 465–469. [CrossRef]
56. Rappaz, M.; Bellet, M.; Deville, M.; Snyder, R. *Numerical Modeling in Materials Science and Engineering*; Springer: Berlin/Heidelberg, Germany, 2002; Volume 32. [CrossRef]
57. ESI. *ProCast User Manual e Technical Reference, Version 6.1*; ESI Software: Rungis, France, 2007.
58. Torroba, A.J.; Koeser, O.; Calba, L.; Maestro, L.; Carreno-Morelli, E.; Rahimian, M.; Milenkovic, S.; Sabirov, I.; Llorca, J. Investment casting of nozzle guide vanes from nickel-based superalloys: Part I—Thermal calibration and porosity prediction. *Integr. Mater. Manuf. Innov.* **2014**, *3*, 344–368. [CrossRef]
59. Dantzig, J.A.; Rappaz, M. *Solidification*; EPFL-Press: Lausanne, Switzerland, 2009.
60. Launder, B.E.; Spaulding, D.B. The Numerical Computation of Turbulent Flows. *Comput. Methods Appl. Mech. Eng.* **1974**, *3*, 269–289. [CrossRef]
61. Kumar, R.; Madhu, S.; Aravindh, K.; Jayakumar, V.; Bharathiraja, G.; Muniappa, A. Casting design and simulation of gating system in rotary adaptor using procast software for defect minimization. *Mater. Today Proc.* **2020**, *22*, 799–805. [CrossRef]
62. Rajkolhe, R.; Khan, J.G. Defects, Causes and Their Remedies in Casting Process: A Review. *Int. J. Res. Advent Technol.* **2014**, *2*, 375–386. Available online: https://ijrat.org/downloads/Vol-2/march-2014/paper%20ID-232014109.pdf (accessed on 12 March 2023).
63. Ingle, V.; Sorte, M. Defects, Root Causes in Casting Process and Their Remedies: Review. Vaibhav Ingle. *Int. J. Eng. Res. Appl.* **2017**, *7*, 47–54. [CrossRef]

Disclaimer/Publisher's Note: The statements, opinions and data contained in all publications are solely those of the individual author(s) and contributor(s) and not of MDPI and/or the editor(s). MDPI and/or the editor(s) disclaim responsibility for any injury to people or property resulting from any ideas, methods, instructions or products referred to in the content.